Carbon 179 (2021) 531–540

Contents lists available at ScienceDirect

Carbon

journal homepage: www.elsevier.com/locate/carbon

Doping and plasmonic Raman enhancement in hybrid single walled carbon nanotubes films with embedded gold nanoparticles

Anna Wroblewska [a, *], Georgy Gordeev [b], Anna Duzynska [a], Stephanie Reich [b], Mariusz Zdrojek [a]

[a] Faculty of Physics, Warsaw University of Technology, Koszykowa 75, 00-662, Warsaw, Poland
[b] Department of Physics, Freie Universität Berlin, Arnimallee 14, 14195, Berlin, Germany

ARTICLE INFO

Article history:
Received 1 December 2020
Received in revised form
9 April 2021
Accepted 23 April 2021
Available online 29 April 2021

Keywords:
Thin films
Gold nanoparticles
Plasmonic enhancement
Exciton-phonon coupling
Statistical analysis

ABSTRACT

Novel optical hybrid materials can be produced with carbon nanotubes and metallic nanoparticles. Such hybrids may allow coupling between plasmons in metals and excitons in nanotubes. We develop novel hybrid materials in the form of thin films using vacuum filtration, where gold nanoparticles are embedded into the entire volume of the nanotube film, not only on the top of the film. After producing semiconducting and metallic hybrids, we investigate their electronic properties. Free charge carriers in metallic nanoparticles extend into nanotubes, resulting in the doping effect. The doping effect manifests in changes the phonon energy and lifetime, scaling with gold nanoparticle concentration. We implement statistical Raman analysis and determine 20 meV p-doping. The statistical data were cross-correlated with parameters of the 2D and G modes, which helped to clearly disentangle doping and strain. Further, we studied optical properties of the films. The gold nanoparticles enhance the CNTs Raman scattering efficiency. The enhancement is wavelength dependent, as confirmed by resonance Raman spectroscopy on radial breathing modes. The enhancement factors vary from 2 to 3.5 times, with maximum at 1.7 eV. The shapes of enhanced resonance Raman profiles were interpreted with the fifth-order perturbation theory incorporating plasmonic effect.

1. Introduction

Single walled carbon nanotubes (CNTs) are unique one-dimensional crystals with outstanding mechanical and optical properties [1]. It is possible to improve these properties by combining CNTs with zero-dimensional materials such as molecules and nanoparticles (NPs). Particularly interesting is a combination with metallic nanoparticles, which enables near field coupling between plasmons, collective electron oscillations in metals [2] and excitons, optical states in carbon nanotubes [3]. The hybridization of these structures manifests in optical phenomena such as the Purcell effect [4] and surface enhanced Raman scattering [5,6].

Several approaches to combine NPs and individual nanotubes have been successfully demonstrated. The hybrids can be prepared by non-covalent methods, where CNTs and gold (Au) nanoparticles are stabilized in a colloidal suspension using a micelle swelling technique [7,8]. However, such systems are unstable if exposed to a changing environment. Another strategy is to attach gold nanoparticles (AuNPs) onto the CNT surface by covalent chemical methods. The photoinduced [9] and [1 + 2] cycloaddition reactions [10] yield hybrids which were more stable and robust, but require sophisticated treatment. The strategies involving the deposition of plasmonic nano-antennas by lithography result in efficient coupling, however such processes are non-scalable [11,12]. A new scalable and efficient approach where the gold nanoparticles are distributed into the entire volume of the CNT film is of high interest.

A thin film is one of the most popular systems made of CNTs, however most of the properties of individual tubes are changed inside the ensemble. The films made of CNTs allow the scaling of unique mechanical properties from nano-to micro-ranges. The methods of CNT film production recently gained attention due to their ability to create monochiral samples with aligned carbon nanotubes [13]. Such films allow observation of record-high thermal conductivity [14], cross polarized excitations [15] and hyperbolic thermal emission [16]. Carbon nanotubes thin films (aligned

* Corresponding author.
E-mail address: anna.wroblewska@pw.edu.pl (A. Wroblewska).

https://doi.org/10.1016/j.carbon.2021.04.079
0008-6223/

or not-arranged) can find applications in transistors [17,18], solar cells [19,20], gas sensing [21], filters [22] and bio sensing [23]. Architectural changes can further improve CNT films and modify their properties such us optical absorption, charge and heat transport via doping, stress, and other mechanisms of electrostatic interaction [24–26]. Previous works showed that hybrids containing carbon nanotubes with gold nanoparticles were made using drop casting method without thickness control [27] or using covalent modifications of nanotube walls causing defects [28].

In this work we present a thin film hybrid material with novel architecture where gold nanoparticles are embedded in a thin film of carbon nanotubes (Fig. 1) that was prepared using vacuum filtration with control over parameters such as thickness and the concentration of gold nanoparticles, all without causing covalent defects in the nanotube walls. Three different concentrations of gold nanoparticles on two different types of CNT films, metallic and semiconducting, were prepared. We present implementation of Raman mapping and statistical analysis to demonstrate changes in the properties of the CNT thin films that are reflected in the parameters of the main Raman mode (G+, G-, 2D). Using this method, we monitor the doping level or changes in the CNT phonon energies. Moreover, we show that the cross-correlation of the parameters of Raman modes allows further study of the interaction CNT with AuNPs, also resolving the dominant effect (doping vs strain). Gold nanoparticles optically interact with nanotubes by confining electromagnetic radiation. This manifests in surface enhanced Raman scattering (SERS) effect. We observed a wavelength dependent Raman enhancement, with the highest increase of Raman intensity being threefold from the expected found in resonance with a plasmonic mode at 1.72 eV. Microscopic theory incorporating fifth-order perturbation theory was used to reproduce resonance Raman profiles. Our work allows us to understand changes in properties of CNT-AuNPs composites that might be useful for various future applications.

2. Materials and methods

Films preparation: CNT-AuNPs hybrid thin films were fabricated via a vacuum filtration method (Fig. 1) using separated metallic or semiconducting single walled carbon nanotubes from NanoIntegris (purity 99%, tube diameter range 1.2 nm−1.7 nm, mean length ~0.5 μm). First, 1 mg of pure dry M-CNTs or S-CNTs was dispersed in 1% water solution of anionic surfactant (sodium dodecyl sulfate; Carl Roth) using bath sonication. Surfactant particles stick to the nanotube walls and prevent to aggregation of nanotubes in liquid. To separate the homogeneous suspension from bundles of nanotubes, the dispersion was centrifuged at 12 000 rpm for 10 min. Next, the supernatant was decanted and mixed with gold nanoparticles' suspension (MKnano, diameter 20 nm, concentration $7.0 \cdot 10^{11}$ particles/ml, stabilized in water with HAuCl4, 5–15% distribution of the sizes), as follows: for each sample, to the same volume of carbon nanotube suspension was added to the 0.5, 1, 2 ml of gold nanoparticles, respectively (indicated as Au1, Au2 and Au3 later in this work). The mixture was then heated to 70 °C for 15 min and then sonicated for 30 min. This procedure improves the adhesion between gold nanoparticles and nanotubes. Such prepared

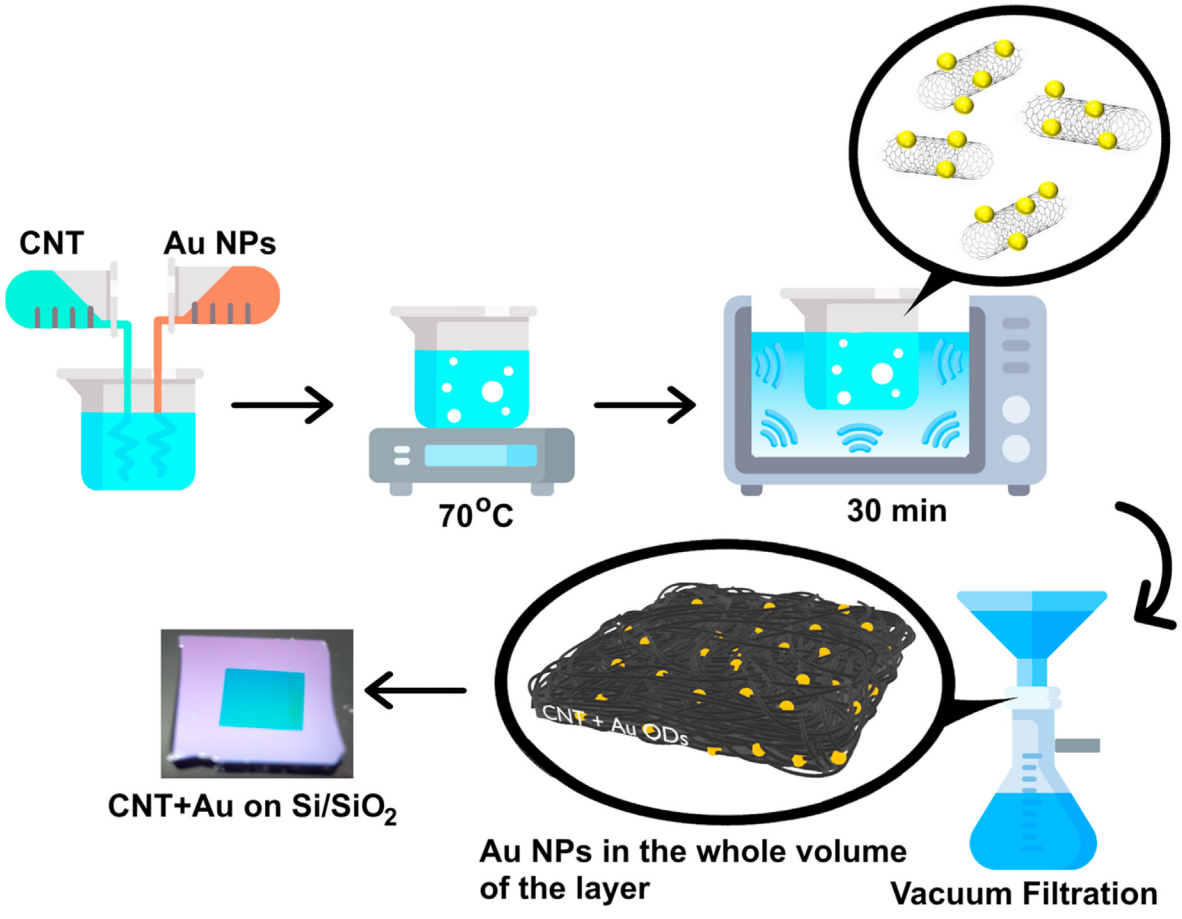

Fig. 1. Schematic illustration of sample production demonstraing how the Au NPs are embedded in a thin film

suspension was filtered through a nanoporous cellulose ester membrane (MCE, 0.025-mm pore size, 25 mm diameter) using a vacuum filtration system (pressure: 0.6 Ba). Residual surfactant and gold nanoparticles' stabilizer were washed away from the CNT-AuNPs film by a large amount of DI water and isopropyl alcohol (comment in Supplementary Information S1–S4). Finally, each CNT-AuNPs hybrid film on vacuum membrane was gently dried, cut for 5 × 5 mm pieces and transferred on SiO2/Si substrate, the cellulose filter was dissolved by acetone vapor. It very special in our method is that it allows for the distribution of gold nanoparticles throughout the whole volume of the CNT film. M-CNT and S-CNT films without the addition of gold nanoparticles were used as reference samples (Fig. 2(a)). Shows absorption spectra for different electronic types of films, collected using a PV response analyser PVE300 Bentham). Using sonication and heating of the solution before filtration provided for better adsorption of nanoparticles to the nanotube surface, which allowed for the production of a thin film of carbon nanotubes containing nanoparticles in the entire volume of the layer, not only on the surface (more information: Supplementary Information, S5–S8). A scanning electron microscope (SEM, Raith e-Line Plus SEM with InLens detector) was used to show the arrangement of the tubes within the film (Fig. 2(b)) and deployment of the nanoparticles on the CNT films surface. The thickness of the samples was approximately 50 nm (Bruker Dimension Icon atomic force microscope, Fig. S5 in Supplementary Information).

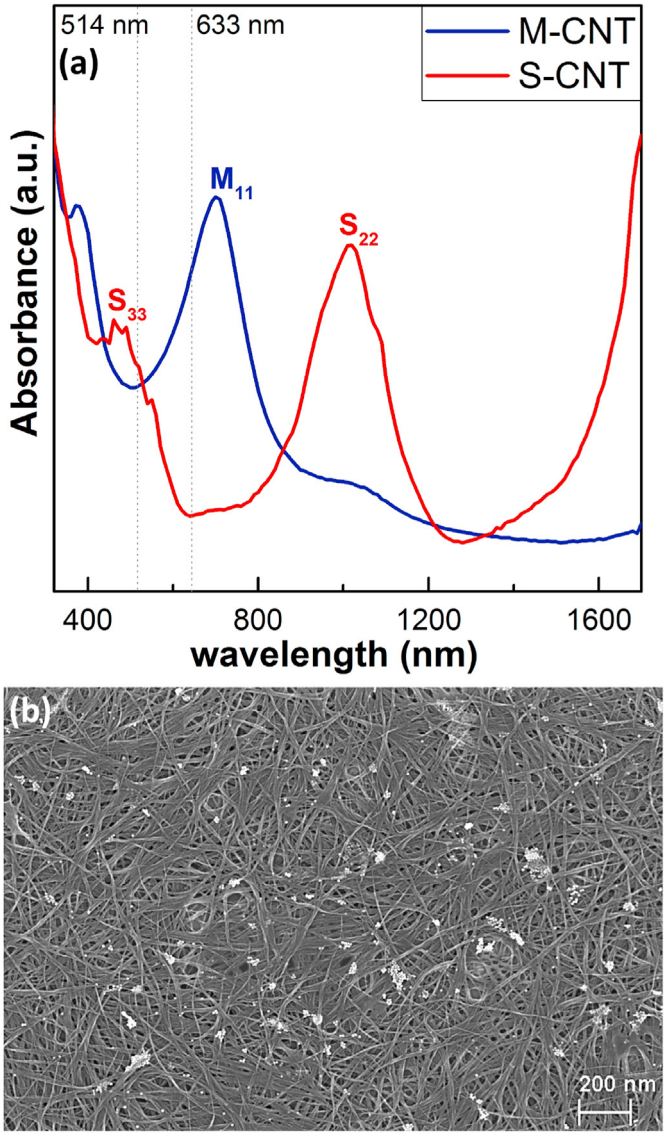

Fig. 2. a) The UV-VIS optical absorption spectrum of single-wall carbon nanotubes: metallic (blue) and semiconducting (red), b) SEM image of carbon nanotube thin film with highest concentration of gold nanoparticles. (A colour version of this figure can be viewed online.)

Statistical Raman analysis: Raman spectra were collected using Renishaw inVia Microscope with 514 nm and 633 nm excitation lines. Measurements were taken in mapping mode with a scan area of 100 μm × 100 μm, that includes 600 single spectra each. To avoid heating effects on the samples during the measurements (more information and comment about heating effect: Supplementary Information, Fig. S6), we used low laser power (~0.35 mW) and unfocused spot on the sample (diameter of laser spot ~4 μm). Measurements were taken at room temperature. Each of single spectra within a map was fit by Lorentzian line shape. All modes parameters: position, intensity and width are then collected in a form of histogram or scatter plots for each given map and samples.

Resonant Raman characterization. The Raman spectra in the radial breathing modes (RBMs) region was recorded for Au3 and pristine films. The light was emitted by a tunable excitation system, a Ti:Sa laser (Coherent MBR 110) providing excitations from 700 to 1000 nm and focused by 100× objective (0.95 N A.) on the CNT films. The samples were excited with 1 mW laser power to avoid sample heating. The backscattered light was collected by the same objective and guided into the spectrometer. A triple grating system of a T64000 Horiba spectrometer equipped with a 900 lines per mm grating and a Peltier cooled Silicon charge coupled device was used to disperse and detect scattered light. Raman shift and intensity were calibrated on Benzonitrile molecules.

3. Results

3.1. Raman mapping and statistical analysis of the impact of gold nanoparticles on metallic CNT thin films

Raman spectroscopy is the most popular tool for the investigation of carbon nanotubes [29–31]. In Raman spectra we can directly see the differences between the metallic and semiconducting species. The electronic type of a CNT is determined by the *(n,m)* chiral indices. Metallic nanotubes correspond to $mod(n-m,3)=0$, all other combination belong to semiconducting electronic type. The band gap of semiconducting nanotubes is proportional to the inverse diameter [32], whereas in metallic nanotubes only *(n,n)* tubes are purely metallic and all other metallic chiralities have small 30–40 meV band gaps [33]. As a result, the LO phonon is coupled to electron yielding a broad peak at 1555.3 cm^{-1} with full width at half maxima (FWHM) = 34 cm^{-1}, see grey area in Fig. 3(a). In contrast, the LO phonon in semiconducting CNTs is relatively narrow (FWHM = 12 cm^{-1}), see peak at 1595 cm^{-1} in Fig. 4(a). Further, we can use Raman spectroscopy to identify the doping effects.

This phonon in metallic carbon nanotubes is highly sensitive to doping effects due to high electron-phonon coupling [34,35]. Therefore, observing the changes in the G^- mode we can report changes in the doping level. Fig. 3(b) shows single Raman spectrum of CNTs thin film with the highest concentration of gold nanoparticles (Au3). One can observe narrowing from 34 cm^{-1} for pristine nanotubes to 29 cm^{-1} after the addition of gold nanoparticles. Furthermore, the position of the G^- mode changes by about 5 cm^{-1}. The changes in the Raman spectrum after the addition of AuNPs is also observed as a broadening (about 1.5 cm^{-1}) and downshifting (from 2635.5 cm^{-1} for pristine nanotubes to

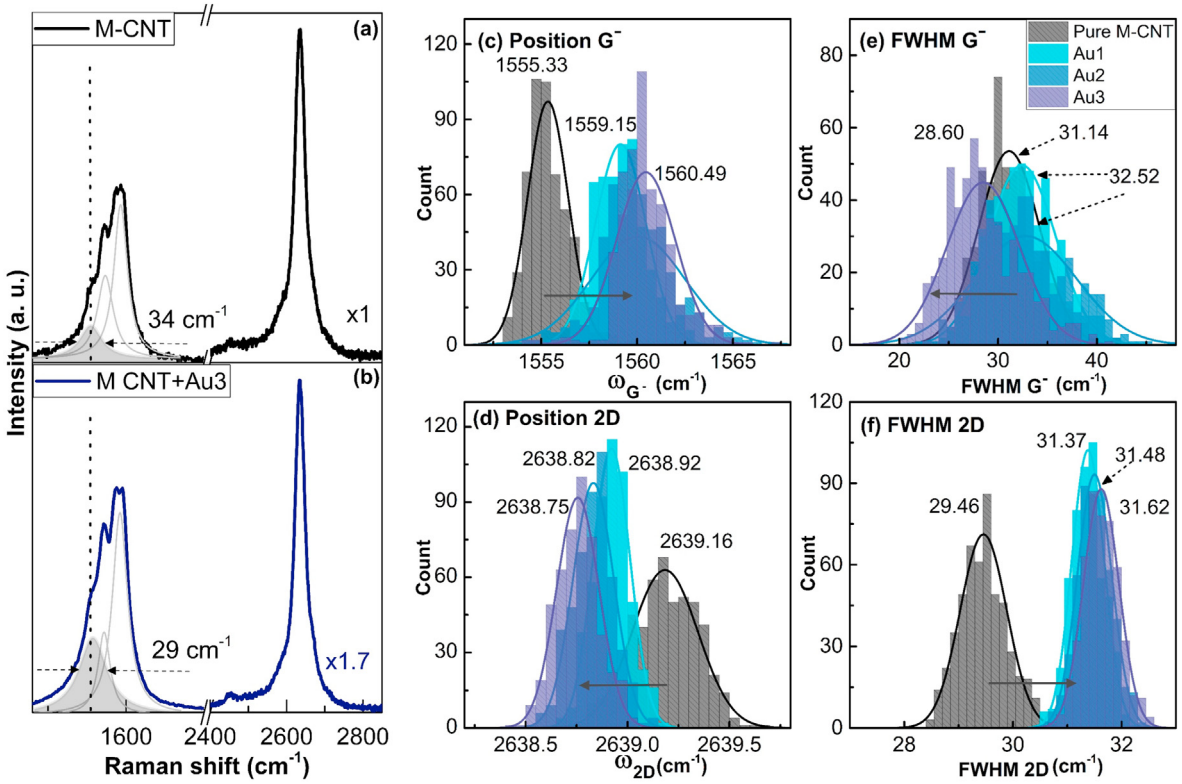

Fig. 3. Raman statistical analysis of metallic CNT films. (a–b) Raman spectrum for pristine metallic (black) and after gold nanoparticles addition (blue) using 633 nm laser line. The grey filled mode marked the analyzed LO phonon, (c–d) histograms of G^- and 2D mode positions and full width at half maximum (FWHM) of the modes (e–f). The mean value of each histogram is determined and labeled by fitting with Gaussian line. The increasing concentration of gold nanoparticles is associated with a darker shade of blue (also marked with an arrow). (A colour version of this figure can be viewed online.)

2634.0 cm^{-1} after gold addition) of the 2D mode. These changes might be an indication of p type doping caused by nanoparticles which leads to the removal of electrons from the valence π bond. As a result, the Fermi level shifts down when compared with the initial value [36,37].

However, based on single spectrum, such fine changes (about 0.5–1.5 cm^{-1} in position or mode width) are difficult to analyse, and thus a statistical approach using Raman maps is proposed. We consider the evolution parameters such as: position and FWHM of the main CNT Raman modes (G^- and 2D) as statistical distribution by preparing histograms. Three different gold nanoparticle concentrations are marked as shades of blue: the brightest corresponds to the smallest concentration (Au1), medium (Au2) and the darkest to indicate the largest concentration (Au3). All results on histograms are compared to a bare film (black). The center position (mean value) of each histogram is marked (after fitting with Gaussian line) and it is further used as a marker for monitoring any changes. In general, the mean value of each histogram has a gradual tendency to shift with an increasing gold NP concentration. All results from the histogram analysis are summarized in Table 1.

Fig. 3(c) and (e) present histograms of the G^- mode position and FWHM in pristine nanotube film and after the addition gold nanoparticles. The position of the G^- mode (Fig. 3(c)) for the pristine CNT films is located at about 1555.33 cm^{-1} and shifts towards higher energies by about 5 cm^{-1} for higher concentration of gold nanoparticles (Au3). Frequency of the LO phonon (Γ point) in metallic nanotubes depends strongest on changes in carrier density. It requires smaller Fermi energy shifts to demonstrate the changes. Nanoparticles attract and partly remove the electrons from the π valence band. The doping impacts the lifetime of zone center G mode phonon as indicated by the changes of the FWHM (G^-). Fig. 3(e) shows the evolution of the FWHM (G^-) histograms as a result of gold nanoparticles addition. We observed a 2.5 cm^{-1} change in the FWHM (G^-) when comparing the average value of the histogram for a pristine CNT layer to one with the highest Gold concentration. We calculated a decrease of the Fermi level by about 20 meV from the G^- mode narrowing [36–39].

The 2D mode can be used to determine the doping type, it represents two phonons from the K point in the Bouillon zone. It is strictly linked with the electronic structure and is sensitive to its changes. Position of the 2D mode for pristine metallic carbon nanotube thin films is about 2639 cm^{-1} and shift to lower energies by about 1.6 cm^{-1} upon the addition of nanoparticles. The direction of the 2D mode shift indicated the p doping [37]. In Fig. 3(f) we present evolution of the FWHM (2D). The FWHM for the thin film of pristine metallic carbon nanotubes was determined to be 29.46 cm^{-1} which becomes broadened to about 31.62 cm^{-1} in the sample with the highest concentration of gold nanoparticles. Broadening of the 2D mode is usually related to charge transfer which can have an effect on double resonance processes. Changes in the resonance condition cause the renormalization of electron and phonon energy, which can affect the 2D mode width [29,37,40].

3.2. Raman mapping and statistical analysis of gold nanoparticles impact on semiconducting CNT thin films

Fig. 4(a) and (b) shows single Raman spectrum for semiconducting CNT thin films with the G and 2D modes of the pristine and Au hybrid thin films. The G mode of semiconducting nanotubes consist of two modes: G^+ (LO), and G^- (TO) and the analyzed LO phonon is marked grey. In contrast to metallic nanotubes, there was no Raman enhancement of the signal due to this excitation being

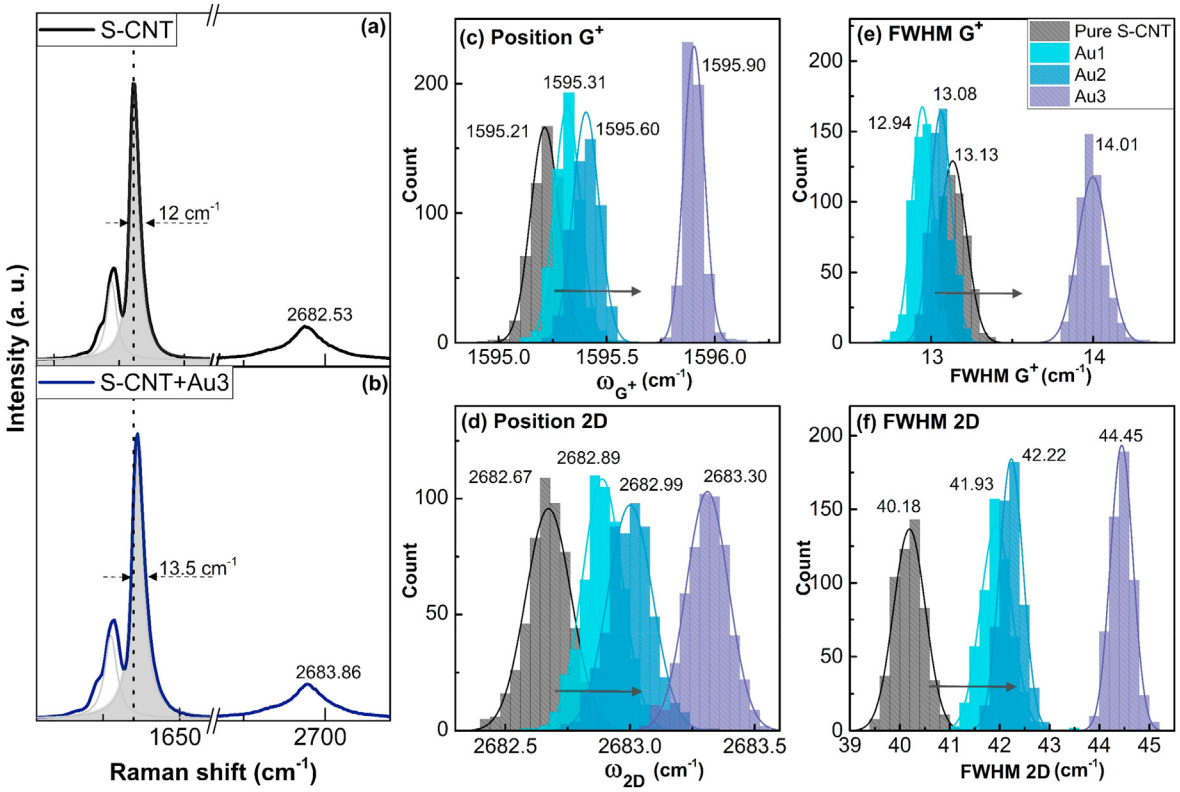

Fig. 4. Raman mapping analysis of the semiconducting CNT films. (a–b) Raman spectrum for the pristine semiconducting thin film (black) and after gold nanoparticles addition (blue) using 514 nm laser line. The grey filled mode marked the analyzed LO phonon. (c–d) histograms of the G^- and 2D mode positions and (e–f) full width at half maximum (FWHM) of the modes. The mean value of each histogram is determined and labeled by fitting with Gaussian line. Increasing concentration of gold nanoparticles is associated with a darker shade of blue (also marked with an arrow). (A colour version of this figure can be viewed online.)

Table 1
Position and FWHM of the G^- and 2D modes shift for pristine metallic carbon nanotube thin film (M-CNT) and hybrid layers with increasing concentration of gold nanoparticles (Au1, Au2, Au3).

	ω_G^- (cm^{-1})	FWHM G^- (cm^{-1})	ω_{2D} (cm^{-1})	FWHM 2D (cm^{-1})
M-CNT	1555.33	31.14	2639.16	29.46
Au1	1559.15	28.60	2638.92	31.37
Au2	1560.49	32.52	2638.82	31.48
Au3	1560.49	32.52	2638.75	31.62

far from plasmon resonance, we will discuss plasmonic effects in the last section. In semiconducting nanotubes after gold nanoparticles were added, a widening and a shift to higher energies of both main modes; the G+ and 2D modes were observed. We attribute these changes again to doping effect.

The histograms of the G^+ mode positions are shown in Fig. 4(c). The G^+ mode for pristine CNT films is about 1596 cm^{-1}. For semiconducting CNTs films the G^+ mode position gradually increases by about 0.1 cm^{-1} for the lowest gold concentration and achieving the most significant change (about 0.7 cm^{-1} and position 1595.90 cm^{-1}) for the highest concentration of gold (marked as Au3). The changes in the G^+ mode position may be associated with charge transfer between CNTs and nanoparticles and has already been shown in extensive studies of the alkali metals on carbon nanotubes [41]. Full width at half maximum of the G^+ mode for pristine layers has a value of about 13 cm^{-1} which for the smallest concentration of gold nanoparticles slightly decreases (12.94 cm^{-1}), but with increasing concentration of nanoparticles, begins to increase to 14.01 cm^{-1} for the highest gold concentration. The LO phonon (the G^+ mode for semiconducting nanotubes) is sensitive to carrier concentration. We estimate an increase of the Fermi level by about 20 meV [29,34,36,39,42].

In Fig. 4 (d) and (f) we present histograms of the 2D mode positions and FWHMs, respectively. For the pristine semiconducting carbon nanotubes thin film, the 2D mode position is at 2682.67 cm^{-1} and shifts gradually with increasing concentrations of nanoparticles to higher energies by about 0.63 cm^{-1}. The position of the 2D band shifts with p- and n-doping in carbon nanotubes [43]. Increasing the mode position could be related to hole doping same as we observed in metallic nanotubes, which results in the removal of electrons from the nanotube valence mode [36,44]. In Fig. 4(f) we show evolution of the 2D mode broadening. The FWHM for the thin film pristine semiconducting CNTs was about 40 cm^{-1} and as it was evolving until a value about 44.45 cm^{-1} for the highest concentration of gold. For increasing levels of hole doping, the Fermi level decreases (in this case of about 0.02 eV) [29,36,42–44]. All data from the histograms for semiconducting thin films are summarized in Table 2.

Table 2
Position and FWHM of the G^+ and 2D modes shift for pristine semiconducting carbon nanotube thin film (S-CNT) and hybrid layers with increasing concentration of gold nanoparticles (Au1, Au2, Au3).

	ω_G^+ (cm^{-1})	FWHM G^+ (cm^{-1})	ω_{2D} (cm^{-1})	FWHM 2D (cm^{-1})
S-CNT	1595.21	13.13	2682.67	40.18
Au1	1595.31	12.94	2682.89	41.18
Au2	1595.60	13.08	2682.99	42.22
Au3	1595.90	14.01	2683.30	44.45

3.3. Cross correlation analysis

The histograms and analysis of the mode positions were the first step in interpreting the impact of gold nanoparticles on carbon nanotube thin film. Further information about the CNTs hybrids can be derived from Raman mode parameters; FWHM combined with mode positions and presented as scatter plots. Similar plots were used previously to obtain information about doping or defects in graphene [45]. Fig. 5 shows statistical evolution (scatter plots) of the position and the FWHM (2D) mode as a function of the LO phonon: G^+ for semiconducting and G^- in metallic films. Correlations are presented for the pristine CNT thin film (CNT) and films with nanoparticles (Au1, Au2, Au3). The grey grid lines in Fig. 5 (a) and (c) are determined from previous stress and doping experiments [36,37,46] which indicate the evolution of peak parameters related to these effects.

Fig. 5(a) and (b) show evolution of the 2D mode position and FWHM (2D) plotted as a function of the G^- mode position for metallic films (with/without gold nanoparticles). This correlation highlights the doping effect of the CNTs, due to characteristic properties of these two modes: the G^- mode reflects the charge transfer between carbon nanotubes and dopants, and the 2D mode is sensitive to changes in local electronic structure such as: carrier density of π mode of nanotubes and the softening or hardening C—C bonds due to charge transfer. In Fig. 5 (a) we show the scatter plots that shift to higher energies of the G^- mode with increasing nanoparticles' concentration and downshift in the 2D mode position. This dependency can reflect the changes in density of sidewall π electrons in carbon nanotubes in the films. One can see that scatter plots for metallic CNT thin films with gold nanoparticles evolve in opposite direction compared to stress/doping grid lines. It could demonstrate only doping effect and no strain.

The 2D mode width plotted as a function of the G^- mode position increases with the concentration of nanoparticles (Fig. 5(b)). This could be related to the hardening of C—C bonds due to changes in carrier density of CNTs π-mode [36,47,48]. Based on previous studies concerning the doping effect in metallic nanotubes (e.g. Refs. [36,46–48]) and prepared grid lines related to doping effect, one can see that the experimental data (scatter plots based on Raman maps) does not represent good enough doping grid lines. Our grid lines follow general trend but some points deviate. This indicates that the 2D width is not purely regulated by doping, but also a change of resonance conditions for different chiralities may contribute to the width of the 2D mode. We will study the optical resonances in the next section.

We performed similar analysis for semiconducting nanotubes, Fig. 5(c) and (d) show scatter plots of the 2D mode position and FWHM plotted against the G^+ position for CNT and AU-CNT films. In Fig. 5(c) we show the scatter plots that shift to higher energies of both modes (G^+ and 2D) with increasing nanoparticles' concentration. This suggests that addition of metallic NPs to the semiconducting tubes causes doping [43]. The width of the 2D mode seems to exhibit similar changes as the G^+ mode width upon addition of NPs. For semiconducting nanotubes (Fig. 5 (d)) the 2D mode width increase (with increase of the G^+ mode position) [36,47]. Grid lines indicate the direction of change characteristic of the occurrence of doping and stress effects. Based on that, one can observe that scatter plots are relatively well covered with the grid

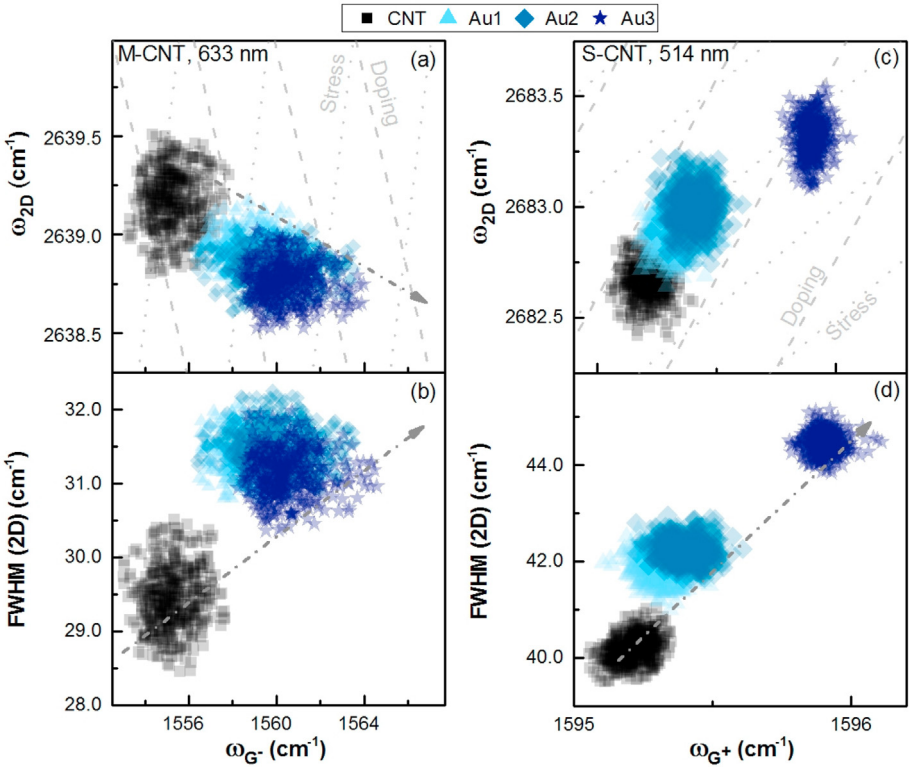

Fig. 5. Scatter plots of main Raman modes. Correlations of: (a) 2D mode position (ω_{2D}) plotted against G^- mode position (ω_G^-) and (b) FWHM (2D) plotted against G^- mode position (ω_G^-) for metallic carbon nanotubes thin film taken at 633 nm laser excitation wavelength. (c) 2D mode position (ω_{2D}) plotted against G^+ mode position (ω_G^+) and (d) FWHM (2D) plotted against G^+ mode position (ω_G^+) for semiconducting carbon nanotubes thin film using a 514 nm laser excitation wavelength. Each point represents single spectra from given Raman map. Pristine carbon nanotube thin film assigned as black squares and hybrid films with increasing concentration marked as: light blue triangle (Au1)- smallest concentration, medium blue rhomb (Au2)- medium concentration and darker blue star (Au3)- highest concentration. Dashed lines with arrow added to guide the eye to indicate the direction of changes with gold concentration. (A colour version of this figure can be viewed online.)

lines. Only the sample with the highest concentration of gold nanoparticles inside layer (Au3) shows a significant deviation from the trend, but there may be combined effects: doping with stress. In the higher doping range, the correlation might no longer linear.

Finally, by comparing correlative plots in metallic and semiconducting nanotubes, Fig. 5 (a) and (c) we find that the slops have different signs. This behavior is expected for the p doping and is a strong indication that doping dominates over stress in the hybrid films. Stress causes the 2D and G modes shifts in the same directions in metallic and semiconducting CNTs. After establishing the electronic effect provided by metallic nanoparticles we can study the optical properties of the hybrid films and specifically Raman enhancement effect.

3.4. Effect of Raman enhancement provided by gold nanoparticles

In semiconducting films no Raman enhancement is observed, see Fig. 4(a). This indicates that the plasmonic resonance is far from 2.3 eV. In the G mode in metallic nanotubes however we observe a 1.6 enhancement at 1.9 eV excitation. We further test wavelength selectivity of Raman enhancement using resonance Raman spectroscopy of radial breathing modes.

Fig. 6(a) and (b) shows Radial breathing modes of pristine and Au3 metallic films excited at 1.65 eV in resonance with absorbance maximum. Overall spectrum consists of many different radial breathing modes each representing a single *(n,m)* species (highlighted in grey). The frequencies of RBMs match expected frequencies [49] with small deviations up to 1 cm^{-1}, see Table 3. Vertical lines in Fig. 6(a) demonstrate the highest (18,0) and lowest (13,10) positions of the 2 $m + n = 36$ laola family [49].

First, we determine the transition energies of CNTs inside the pristine thin film by applying resonance Raman spectroscopy. The calibrated intensity of each RBM with (grey) is plotted over excitation energy in Fig. 6(c–e). The intensity of the RBM mode increases when laser energy approaches excitonic resonance of metallic nanotubes. The intensity of an RBM depends on laser energy (E_L) as described by the third-order perturbation theory equation [49,50]:

$$I_{RBM}(E_L) \sim \left| \frac{M_{CNT}}{\left(E_L - E_{11}^L - \hbar\omega_{RBM} - i\frac{\Gamma}{2}\right)\left(E_L - E_{11}^L - i\frac{\Gamma}{2}\right)} \right|^2, \quad (1)$$

where M_{CNT} is the matrix element combining exciton-photon and exciton-phonon coupling. E_{11}^L is the energy of the second excitonic state and Γ is the broadening factor related to the finite lifetime of the exciton. The Raman profile of the Stokes scattering comprises two resonances incoming at E_{11} and outgoing at $E_{11} + \hbar\omega_{RBM}$, where with a small phonon energy ($\hbar\omega_{RBM}$) these resonances are unresolved and maximum Raman intensity occurs between them [50]. In metallic nanotubes two transition with the same index have similar energies, one at lower E_{11}^L and the other at higher energy E_{11}^H. Despite having similar oscillator strength the Raman intensity of the E_{11}^H is negligibly small due to weak exciton-phonon coupling [51,52].

By fitting experimental resonance Raman profiles in Fig. 6(e–c) by Eq. (1) (full grey lines) we obtain parameters of the pristine tubes inside the films. These parameters are listed in Table 1. An average broadening factor comprises 120 meV exceeding by a factor of two typical broadening of suspended single-walled nanotubes (50 meV) [50]. This is related to decrease lifetime in the nonhomogeneous bundles. Furthermore, the transition energy E_{11}^L is blue-shifted compared to the suspended tubes. The bundling can induce up to 50 meV shift to smaller energies, whereas residual effect can be related to strain. The effects of strain oriented along the tube axis (uniaxial) on electronic bandgaps strongly depend on chiral angle. By expansive strain and the E_{11}^L transition a displacement to lower energies proportional to $Cos(3\theta)$ is expected, where θ is a chiral angle of the tube. Indeed in (18,0) the transition energy moves by 15 meV, whereas in (13,10) the shift to smaller energies is much larger ~70 meV.

3.5. Quantifying the surface Raman enhancement effect

Raman scattering intensity of an object in a vicinity of a rough metal surface may be enhanced by interaction with collective electronic excitations (plasmons) within metals [5,6]. In our system, the gold nanoparticles form near-field cavities and Raman response of nanotubes is probed in order to identify a plasmonic resonance. Same as for pristine sample each RBM is *(n,m)* index identified in the Au3 samples, see Fig. 6(b). The intensities of the corresponding modes are compared for pristine (grey) and Au3 (blue) samples in Fig. 6(c–f). The effect of Raman enhancement is most prominent in (14,6) nanotube, where the RBM intensity increases by up to 3.5 times, see Fig. 6(e).

In order to quantify the enhancement we treat plasmonic enhancement as a higher-order Raman process [53]. Two additional interactions (perturbations) [54] with the plasmon need be introduced into the third-order perturbation theory, Eq. (1). These interactions occur twice during Raman scattering process by in- and out-coupling of the light. Resulted formula represents fifth-order perturbation theory and is given by Ref. [55]:

$$I_{RBM}(E_L) \sim \left| \frac{M_{CNT}\, M_{Pl}}{\left(E_L - E_{11}^L - \hbar\omega_{RBM} - iy_{CNT}/2\right)\left(E_L - E_{11}^L - iy_{CNT}/2\right)\left(E_L - E_{Pl} - \hbar\omega_{RBM} - iy_{pl}/2\right)\left(E_L - E_{Pl} - iy_{pl}/2\right)} \right|^2, \quad (2)$$

where M_{CNT}, E_{11}^L, $\hbar\omega_{RBM}$, y_{CNT} refer to intrinsic properties of the nanotubes. The M_{Pl}, E_{Pl}, and y_{pl} are the matrix elements, the energy and broadening of plasmonic resonance, respectively. Full blue lines in Fig. 6(c–f) represent fits by Eq. (2), where intrinsic parameters of the nanotubes were fixed to the values determined for pristine samples (Eq. (1)). The matrix elements of pristine nanotube M_{CNT} are compared with plasmonic ones M_{CNT} in Fig. 6(h). The Raman signals of all the nanotubes with transition energies above 1.65 eV are enhanced. The nanotubes resonant at 1.67 eV demonstrate a superior enhancement, indicating the centre of plasmonic resonance. However, plasmonic broadening $y_{pl}/2$ is quite large ~0.21 eV compared to systems with coupled nanoparticles [56]. We attribute that to an inhomogeneous broadening effect where nanoparticles of different diameters and cavities of different width

(distances between NPs) contribute to the signal. A homogeneous nanotube chirality and a finer control over the NP size and concentration will yield higher matrix elements ($M_{Plasmon}$) and narrower broadening (y_{pl}). $M_{Plasmon}$ contains several parameters of the system [57], the most important factor is oscillator strength of the plasmonic particle which scales with electron concentration and nanoparticle volume. Further the orientation between plasmonic mode and CNT transition dipole and distance between them play an important role. And finally, $M_{Plasmon}$ decays with increased dielectric screening. A decreased average distance between plasmonic antenna and single CNT is equivalent to NP concentration increase in the context of CNT-NP hybrid film. Another strategy to improve the enhancement can be based on larger NPs size, i.e. increasing oscillator strength.

4. Discussion

Carbon nanotubes thin films became one of the most intensely studied material for the nanoscience research and applications over last few decades. We are currently at a pivotal moment in understanding and control of such materials. Here, we introduced the statistical approach for optically measuring the doping effect on order of meV. This approach can be applied in all the types of systems containing carbon nanotubes such as functionalized nanotubes [58,59], filled nanotubes [60], and other types of nanotube composites [61]. Secondly, we presented the nanoparticle-nanotube hybrid films and studied their optical properties. In the hybrid the Raman scattering intensity enhanced due to coupling between plasmons and excitons. This coupling can be improved by optimizing the hybrid components. For instance, one can use pre-

Table 3
Surface resonance enhanced Raman scattering effect in Metallic nanotubes-gold nanoparticles hybrids and analyzed for the $2n + m = 36$ laola family. *(n,m)* indices of corresponding species E_{11}^{L} are taken from Ref. [51]. (*CNT*) index refers to pristine sample, see Eq. (1), whereas (*pl*) index refers to Au3 plasmonic system, see Eq. (2).

(n,m)	RBM, cm^{-1}	E_{11}^{L} [51], eV	E_{11}^{L} Film, eV	E_{Pl}, eV	M_{CNT}, arb. u.	$M_{Plasmon}$, arb. u.	y_{CNT}, meV	y_{pl}, meV
(13,10)	155	1.69	1.62	1.63	2.9	2.7	148.5	200
(14,8)	160.3	1.71	1.67	1.67	4.6	6.8	137.5	200
(15,6)	164.5	1.72	1.67	1.67	3.3	6.8	102.7	240
(16,4)	167.8	1.73	1.71	1.70	3.8	7.5	109.4	220
(17,2)	169.8	1.74	1.72	1.71	4.0	6.9	105.9	240
(18,0)	170.5	1.74	1.72	1.71	4.0	6.9	105.9	240

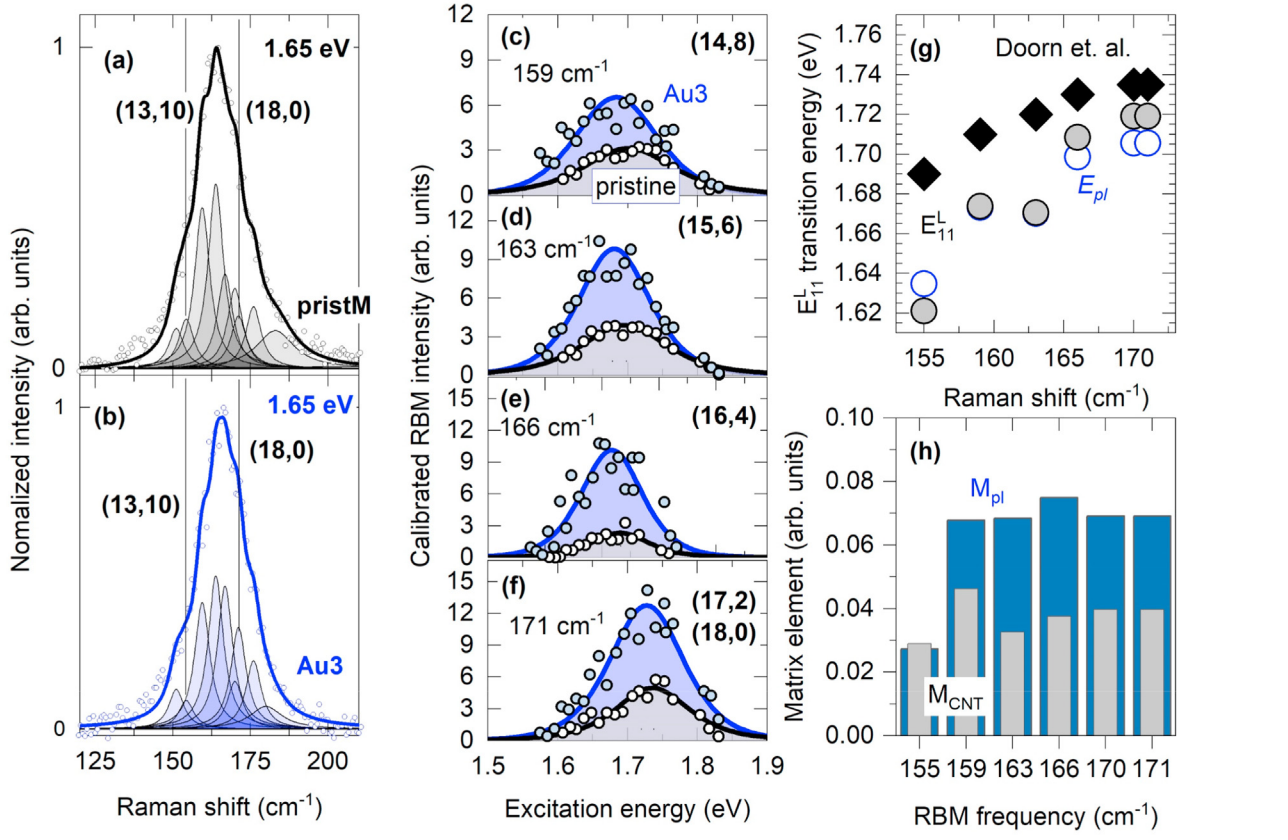

Fig. 6. Resonance Raman spectroscopy of pristine (grey) and Au3 hybrid metallic CNT films (blue). (a) Raman spectrum in the RBM mode range for (a) pristine metallic and (b) Au3 nanotubes with constituent RBMs (filled modes) excited at 1.65 eV. (c–f) Resonance Raman profiles for $2n + m = 36$ laola family where calibrated RBM intensity is plotted versus excitation energy for pristine (grey) and Au3 hybrid (blue) CNT films. Symbols represent experimental data and lines fits by Eq. (1) (grey) and Eq. (2) (blue). The chiral indices *(n,m)* (RBM frequency) are specified in the right (left) top corner. (g) Kataura plots, where transition energy is plotted over RBM frequency, the grey circles represent experimental data for E_{11}^{L} transition, black diamonds Ref. [51], open circles E_{Pl}. (h) A histogram comparing matrix elements of pristine nanotube M_{CNT} with plasmonic system M_{Pl}, see Eqs. (1) and (2). (A colour version of this figure can be viewed online.)

separated [52,62,63] single chirality nanotubes and the nanoparticle with the overlapping plasmonic resonance. Additionally, the concentration of nanoparticles can be increased. In such configurations, the Raman enhancement factors can be increased by orders of magnitude. We envisage our hybrids to improve the performance of CNT based devices, such as transistors [17,18], solar cells [19,20], gas sensors [21], filters [22] and bio sensors [23].

5. Conclusions

In this work, we have introduced the method of producing a material containing gold nanoparticles in the whole volume of the layer. We also presented utilization of Raman mapping to scan large areas of the samples and statistical analysis to investigate properties reflected in the main Raman modes: G^+, G^-, 2D. Histograms of band positions allowed to observe the p-type doping, which is an effect already observed for carbon nanotubes and gold nanoparticles. We used a new cross-sectional analysis to improve metrology in establishing doping and stain effects in CNT based systems. Moreover, resonance Raman spectroscopy of radial breathing modes allowed the determination of transition energies of carbon nanotubes thin films (pure and hybrid layers). By fitting experimental resonance Raman profiles we designated an average broadening factor as 120 meV, which is an over two times larger than for two of three suspended single-walled nanotubes (typical broadening about 50 meV). Gold nanoparticles optically interact with nanotubes as surface enhanced Raman scattering (SERS) effect. Resonance Raman spectroscopy of Radial breathing modes reported up to 3.5 times Raman enhancement factors compared with films without gold nanoparticles. The shapes of the resonance Raman profiles were analyzed with a fifth-order perturbation theory framework. This work improves our understanding of CNT-AuNPs composites and paves a path to its modifications and applications.

CRediT authorship contribution statement

Anna Wroblewska: Investigation, Methodology, Formal analysis, Writing – original draft. **Georgy Gordeev:** Investigation, Methodology, Formal analysis, Writing – original draft. **Anna Duzynska:** Validation, Methodology, Writing – review & editing. **Stephanie Reich:** Resources, Supervision, Writing – review & editing, Funding acquisition. **Mariusz Zdrojek:** Conceptualization, Resources, Supervision, Writing – review & editing, Funding acquisition.

Declaration of competing interest

The authors declare that they have no known competing financial interests or personal relationships that could have appeared to influence the work reported in this paper.

Acknowledgment

We thank Michał Świniarski for his help with SEM imaging. A.W. acknowledges support by the PROM PW project, financed by the European Social Fund under the Operational Program Knowledge Education Development (POWR.03.03.00–00-PN13/18). G.G. and S.R. acknowledge Focus Area NanoScale of Freie Universitaet Berlin. S. R. acknowledges support by the Deutsche Forschungsgemeinschaft under SPP 2244. We thank Oisín Garrity for language corrections. Icons in Fig. 1 made by Freepik from www.flaticon.com.

Appendix A. Supplementary data

Supplementary data to this article can be found online at https://doi.org/10.1016/j.carbon.2021.04.079.

References

[1] S. Reich, C. Thomsen, J. Maultzsch, Carbon Nanotubes : Basic Concepts and Physical Properties, WILLEY-VCH, New York, 2004, ISBN 978-3-527-40386-8.
[2] M.A. Garcia, Surface plasmons in metallic nanoparticles: fundamentals and applications, J. Phys. D Appl. Phys. 45 (2012), https://doi.org/10.1088/0022-3727/45/38/389501.
[3] F. Wang, G. Dukovic, L.E. Brus, T.F. Heinz, The Optical Resonances in Carbon nanotubes arise from excitons, Science 308 (80) (2005) 838–841, https://doi.org/10.1126/science.1110265.
[4] Y. Luo, E.D. Ahmadi, K. Shayan, Y. Ma, K.S. Mistry, C. Zhang, J. Hone, J.L. Blackburn, S. Strauf, Purcell-enhanced quantum yield from carbon nanotube excitons coupled to plasmonic nanocavities, Nat. Commun. 8 (2017), https://doi.org/10.1038/s41467-017-01777-w.
[5] M.G. Albrecht, J.A. Creighton, Anomalously intense Raman spectra of pyridine at a silver electrode, J. Am. Chem. Soc. 99 (1977) 5215–5217, https://doi.org/10.1021/ja00457a071.
[6] D.L. Jeanmaire, R.P. Van Duyne, Surface Raman spectroelectrochemistry. Part I. Heterocyclic, aromatic, and aliphatic amines adsorbed on the anodized silver electrode, J. Electroanal. Chem. 84 (1977) 1–20, https://doi.org/10.1016/S0022-0728(77)80224-6.
[7] M. Glaeske, A. Setaro, Effect of hybrid isolation on the luminescence enhancement of carbon nanotube-gold nanorod composites, Phys. Status Solidi Basic Res. 251 (2014) 2480–2484, https://doi.org/10.1002/pssb.201451288.
[8] M. Glaeske, A. Setaro, Nanoplasmonic colloidal suspensions for the enhancement of the luminescent emission from single-walled carbon nanotubes, Nano Res 6 (2013) 593–601, https://doi.org/10.1007/s12274-013-0335-5.
[9] H. Ismaili, F. Lagugné-Labarthet, M.S. Workentin, Covalently assembled gold nanoparticle-carbon nanotube hybrids via a photoinitiated carbene addition reaction, Chem. Mater. 23 (2011) 1519–1525, https://doi.org/10.1021/cm103284g.
[10] A. Setaro, M. Adeli, M. Glaeske, D. Przyrembel, T. Bisswanger, G. Gordeev, F. Maschietto, A. Faghani, B. Paulus, M. Weinelt, R. Arenal, R. Haag, S. Reich, Preserving π-conjugation in covalently functionalized carbon nanotubes for optoelectronic applications, Nat. Commun. 8 (2017) 1–7, https://doi.org/10.1038/ncomms14281.
[11] S. Heeg, A. Oikonomou, R. Fernandez-Garcia, C. Lehmann, S.A. Maier, A. Vijayaraghavan, S. Reich, Plasmon-enhanced Raman scattering by carbon nanotubes optically coupled with near-field cavities, Nano Lett. 14 (2014) 1762–1768, https://doi.org/10.1021/nl404229w.
[12] Y. Zakharko, A. Graf, J. Zaumseil, Plasmonic crystals for strong light-matter coupling in carbon nanotubes, Nano Lett. 16 (2016) 6504–6510, https://doi.org/10.1021/acs.nanolett.6b03086.
[13] X. He, W. Gao, L. Xie, B. Li, Q. Zhang, S. Lei, J.M. Robinson, E.H. Hroz, S.K. Doorn, W. Wang, R. Vajtai, P.M. Ajayan, W.W. Adams, R.H. Hauge, J. Kono, Wafer-scale monodomain films of spontaneously aligned single-walled carbon nanotubes, Nat. Nanotechnol. 11 (2016) 633–638, https://doi.org/10.1038/nnano.2016.44.
[14] S. Yamaguchi, I. Tsunekawa, N. Komatsu, W. Gao, T. Shiga, T. Kodama, J. Kono, J. Shiomi, One-directional thermal transport in densely aligned single-wall carbon nanotube films, Appl. Phys. Lett. 115 (2019), https://doi.org/10.1063/1.5127209.
[15] F. Katsutani, W. Gao, X. Li, Y. Ichinose, Y. Yomogida, K. Yanagi, J. Kono, Direct observation of cross-polarized excitons in aligned single-chirality single-wall carbon nanotubes, Phys. Rev. B 99 (2019), 035426, https://doi.org/10.1103/PhysRevB.99.035426.
[16] W. Gao, C.F. Doiron, X. Li, J. Kono, G.V. Naik, Macroscopically aligned carbon nanotubes as a refractory platform for hyperbolic thermal emitters, ACS Photonics 6 (2019) 1602–1609, https://doi.org/10.1021/acsphotonics.9b00452.
[17] M. Rother, M. Brohmann, S. Yang, S.B. Grimm, S.P. Schießl, A. Graf, J. Zaumseil, Aerosol-jet printing of polymer-sorted (6,5) carbon nanotubes for field-effect transistors with high reproducibility, Adv. Electron. Mater. 3 (2017), https://doi.org/10.1002/aelm.201700080.
[18] M. Brohmann, F.J. Berger, M. Matthiesen, S.P. Schießl, S. Schneider, J. Zaumseil, Charge transport in mixed semiconducting carbon nanotube networks with tailored mixing ratios, ACS Nano (2019), https://doi.org/10.1021/acsnano.9b03699.
[19] I. Jeon, K. Cui, T. Chiba, A. Anisimov, A.G. Nasibulin, E.I. Kauppinen, S. Maruyama, Y. Matsuo, Direct and dry deposited single-walled carbon nanotube films doped with MoOx as electron-blocking transparent electrodes for flexible organic solar cells, J. Am. Chem. Soc. 137 (2015) 7982–7985, https://doi.org/10.1021/jacs.5b03739.
[20] I. Jeon, R. Xiang, A. Shawky, Y. Matsuo, S. Maruyama, Solar cells: single-walled carbon nanotubes in emerging solar cells: synthesis and electrode applications (adv. Energy mater. 23/2019), Adv. Energy Mater. 9 (2019), 1970091, https://doi.org/10.1002/aenm.201970091.

[21] M.P.N. Bui, S. Lee, K.N. Han, X.H. Pham, C.A. Li, J. Choo, G.H. Seong, Electrochemical patterning of gold nanoparticles on transparent single-walled carbon nanotube films, Chem. Commun. (2009) 5549–5551, https://doi.org/10.1039/b906939a.
[22] F.J. Berger, T.M. Higgins, M. Rother, A. Graf, Y. Zakharko, S. Allard, M. Matthiesen, J.M. Gotthardt, U. Scherf, J. Zaumseil, From broadband to electrochromic notch filters with printed monochiral carbon nanotubes, ACS Appl. Mater. Interfaces 10 (2018) 11135–11142, https://doi.org/10.1021/acsami.8b00643.
[23] T.P. McNicholas, K. Zhao, C. Yang, S.C. Hernandez, A. Mulchandani, N.V. Myung, M.A. Deshusses, Sensitive detection of elemental mercury vapor by gold-nanoparticle- decorated carbon nanotube sensors, J. Phys. Chem. C 115 (2011) 13927–13931, https://doi.org/10.1021/jp203662w.
[24] S.B. Yang, B.S. Kong, H.T. Jung, Multistep deposition of gold nanoparticles on single-walled carbon nanotubes for high-performance transparent conducting films, J. Phys. Chem. C 116 (2012) 25581–25587, https://doi.org/10.1021/jp3080332.
[25] J.L. Xu, R.X. Dai, Y. Xin, Y.L. Sun, X. Li, Y.X. Yu, L. Xiang, D. Xie, S.D. Wang, T.L. Ren, Efficient and reversible electron doping of semiconductor-enriched single-walled carbon nanotubes by using decamethylcobaltocene, Sci. Rep. 7 (2017), https://doi.org/10.1038/s41598-017-05967-w.
[26] M.M. Rabbani, D. Kim, H.C. Kim, C.H. Ko, D.G. Nam, Y.M. Yu, Y. Do Park, W. Oh, Electrostatic interaction of multi-walled carbon nanotubes composites with CdTe and CdSe nanoparticles, Met. Mater. Int. 17 (2011) 227–231, https://doi.org/10.1007/s12540-011-0407-6.
[27] W. Da Silva, M.E. Ghica, C.M.A. Brett, Gold nanoparticle decorated multiwalled carbon nanotube modified electrodes for the electrochemical determination of theophylline, Anal. Methods 10 (2018) 5634–5642, https://doi.org/10.1039/c8ay02150c.
[28] J. Lee, M. Morita, K. Takemura, E.Y. Park, A multi-functional gold/iron-oxide nanoparticle-CNT hybrid nanomaterial as virus DNA sensing platform, Biosens. Bioelectron. 102 (2018) 425–431, https://doi.org/10.1016/j.bios.2017.11.052.
[29] M.S. Dresselhaus, G. Dresselhaus, R. Saito, A. Jorio, Raman spectroscopy of carbon nanotubes, Phys. Rep. 409 (2005) 47–99, https://doi.org/10.1016/j.physrep.2004.10.006.
[30] A.C. Ferrari, Raman spectroscopy of graphene and graphite: disorder, electron-phonon coupling, doping and nonadiabatic effects, Solid State Commun. 143 (2007) 47–57, https://doi.org/10.1016/j.ssc.2007.03.052.
[31] L.M. Malard, M.A. Pimenta, G. Dresselhaus, M.S. Dresselhaus, Raman spectroscopy in graphene, Phys. Rep. 473 (2009) 51–87, https://doi.org/10.1016/j.physrep.2009.02.003.
[32] C. Thomsen, S. Reich, in: C. Manuel, R. Merlin (Eds.), Raman Scattering in Carbon Nanotubes, Light Scatt. Solids IX, Springer, Berlin Heidelberg, 2007, ISBN 978-3-540-34436-0, pp. 164–169.
[33] M. Ouyang, J.-L. Huang, C.L. Cheung, C.M. Lieber, Energy gaps in "metallic" single-walled carbon nanotubes, Science 292 (80) (2001) 702–705, https://doi.org/10.1126/science.1058853.
[34] H. Farhat, H. Son, G.G. Samsonidze, S. Reich, M.S. Dresselhaus, J. Kong, Phonon softening in individual metallic carbon nanotubes due to the Kohn Anomaly, Phys. Rev. Lett. 99 (2007) 1–4, https://doi.org/10.1103/PhysRevLett.99.145506.
[35] A. Das, A.K. Sood, A. Govindaraj, A.M. Saitta, M. Lazzeri, F. Mauri, C.N.R. Rao, Doping in carbon nanotubes probed by Raman and transport measurements, Phys. Rev. Lett. 99 (2007), 136803, https://doi.org/10.1103/PhysRevLett.99.136803.
[36] P. Corio, P.S. Santos, V.W. Brar, G.G. Samsonidze, S.G. Chou, M.S. Dresselhaus, Potential dependent surface Raman spectroscopy of single wall carbon nanotube films on platinum electrodes, Chem. Phys. Lett. 370 (2003) 675–682, https://doi.org/10.1016/S0009-2614(03)00157-X.
[37] B. Hatting, S. Heeg, K. Ataka, J. Heberle, F. Hennrich, M.M. Kappes, R. Krupke, S. Reich, Fermi energy shift in deposited metallic nanotubes: a Raman scattering study, Phys. Rev. B Condens. Matter 87 (2013), 165442, https://doi.org/10.1103/PhysRevB.87.165442.
[38] M.S. Strano, C.B. Huffman, V.C. Moore, M.J. O'Connell, E.H. Haroz, J. Hubbard, M. Miller, K. Rialon, C. Kittrell, S. Ramesh, R.H. Hauge, R.E. Smalley, Reversible, band-gap-selective protonation of single-walled carbon nanotubes in solution, J. Phys. Chem. B 107 (2003) 6979–6985, https://doi.org/10.1021/jp027664a.
[39] G. Gordeev, A. Setaro, M. Glaeske, S. Jürgensen, S. Reich, Doping in covalently functionalized carbon nanotubes: a Raman scattering study, Phys. Status Solidi Basic Res. 253 (2016) 2461–2467, https://doi.org/10.1002/pssb.201600636.
[40] I.O. MacIel, N. Anderson, M.A. Pimenta, A. Hartschuh, H. Qian, M. Terrones, H. Terrones, J. Campos-Delgado, A.M. Rao, L. Novotny, A. Jorio, Electron and phonon renormalization near charged defects in carbon nanotubes, Nat. Mater. 7 (2008) 878–883, https://doi.org/10.1038/nmat2296.
[41] M. Stoll, P.M. Rafailov, W. Frenzel, C. Thomsen, Electrochemical and Raman measurements on single-walled carbon nanotubes, Chem. Phys. Lett. 375 (2003) 625–631, https://doi.org/10.1016/S0009-2614(03)00929-1.
[42] A. Das, A.K. Sood, Renormalization of the phonon spectrum in semiconducting single-walled carbon nanotubes studied by Raman spectroscopy, Phys. Rev. B Condens. Matter 79 (2009), 235429, https://doi.org/10.1103/PhysRevB.79.235429.
[43] S. Grimm, S.P. Schießl, Y. Zakharko, M. Rother, M. Brohmann, J. Zaumseil, Doping-dependent G-mode shifts of small diameter semiconducting single-walled carbon nanotubes, Carbon N. Y. 118 (2017) 261–267, https://doi.org/10.1016/j.carbon.2017.03.040.
[44] P. Corio, A. Jorio, N. Demir, M.S. Dresselhaus, Spectro-electrochemical studies of single wall carbon nanotubes films, Chem. Phys. Lett. 392 (2004) 396–402, https://doi.org/10.1016/j.cplett.2004.05.050.
[45] Q.H. Wang, Z. Jin, K.K. Kim, A.J. Hilmer, G.L.C. Paulus, C.J. Shih, M.H. Ham, J.D. Sanchez-Yamagishi, K. Watanabe, T. Taniguchi, J. Kong, P. Jarillo-Herrero, M.S. Strano, Understanding and controlling the substrate effect on graphene electron-transfer chemistry via reactivity imprint lithography, Nat. Chem. 4 (2012) 724–732, https://doi.org/10.1038/nchem.1421.
[46] S.B. Cronin, A.K. Swan, M.S. Ünlü, B.B. Goldberg, M.S. Dresselhaus, M. Tinkham, Resonant Raman spectroscopy of individual metallic and semiconducting single-wall carbon nanotubes under uniaxial strain, Phys. Rev. B Condens. Matter 72 (2005) 35425, https://doi.org/10.1103/PhysRevB.72.035425.
[47] J.E. Lee, G. Ahn, J. Shim, Y.S. Lee, S. Ryu, Optical separation of mechanical strain from charge doping in graphene, Nat. Commun. 3 (2012) 1024–1028, https://doi.org/10.1038/ncomms2022.
[48] I.F. Herbut, V. Juričić, B. Roy, Theory of interacting electrons on the honeycomb lattice, Phys. Rev. B Condens. Matter 79 (2009) 1–14, https://doi.org/10.1103/PhysRevB.79.085116.
[49] J. Maultzsch, H. Telg, S. Reich, C. Thomsen, Radial breathing mode of single-walled carbon nanotubes: optical transition energies and chiral-index assignment, Phys. Rev. B Condens. Matter 72 (2005), 205438, https://doi.org/10.1103/PhysRevB.72.205438.
[50] G. Gordeev, A. Jorio, P. Kusch, B.G.M. Vieira, B. Flavel, R. Krupke, E.B. Barros, S. Reich, Resonant anti-Stokes Raman scattering in single-walled carbon nanotubes, Phys. Rev. B 96 (2017), 245415, https://doi.org/10.1103/PhysRevB.96.245415.
[51] S.K. Doorn, P.T. Araujo, K. Hata, A. Jorio, Excitons and exciton-phonon coupling in metallic single-walled carbon nanotubes: resonance Raman spectroscopy, Phys. Rev. B Condens. Matter 78 (2008) 1–9, https://doi.org/10.1103/PhysRevB.78.165408.
[52] H. Li, G. Gordeev, O. Garrity, N.A. Peyyety, P.B. Selvasundaram, S. Dehm, R. Krupke, S. Cambré, W. Wenseleers, S. Reich, M. Zheng, J.A. Fagan, B.S. Flavel, Separation of specific single-enantiomer single-wall carbon nanotubes in the large-diameter regime, ACS Nano 14 (2020) 948–963, https://doi.org/10.1021/acsnano.9b08244.
[53] N.S. Mueller, S. Heeg, S. Reich, Surface-enhanced Raman scattering as a higher-order Raman process, Phys. Rev. 94 (2016) 1–13, https://doi.org/10.1103/PhysRevA.94.023813.
[54] P.Y. Yu, M. Cardona, Fundamentals of Semiconductors – Physics and Materials Properties, Springer, Berlin Heidelberg, 1995, https://doi.org/10.1524/zpch.1997.198.Part_1_2.275.
[55] S.T. Waßerroth, Plasmon-enhanced Raman Scattering of Carbon Nanosystems, Freie Universität Berlin, 2019. PhD thesis.
[56] S. Wasserroth, S. Heeg, N.S. Mueller, P. Kusch, U. Hübner, E. Gaufrès, N.Y.W. Tang, R. Martel, A. Vijayaraghavan, S. Reich, Resonant, plasmonic Raman enhancement of α-6T molecules encapsulated in carbon nanotubes, J. Phys. Chem. C 123 (2019) 10578–10585, https://doi.org/10.1021/acs.jpcc.9b01600.
[57] N.S. Mueller, S. Reich, Modeling surface-enhanced spectroscopy with perturbation theory, Front. Chem. 7 (2019) 470, https://doi.org/10.3389/fchem.2019.00470.
[58] A. Setaro, C.S. Popeney, B. Trappmann, V. Datsyuk, R. Haag, S. Reich, Polyglycerol-derived amphiphiles for single walled carbon nanotube suspension, Chem. Phys. Lett. 493 (2010) 147–150, https://doi.org/10.1016/j.cplett.2010.05.052.
[59] A. Hirsch, Functionalization of single-walled carbon nanotubes, Angew. Chem. Int. Ed. 41 (2002) 1853–1859, https://doi.org/10.1002/1521-3773(20020603)41:11<1853::AID-ANIE1853>3.0.CO;2-N.
[60] S. Cambré, B. Schoeters, S. Luyckx, E. Goovaerts, W. Wenseleers, Experimental observation of single-file water filling of thin single-wall carbon nanotubes down to chiral index (5,3), Phys. Rev. Lett. 104 (2010) 207401, https://doi.org/10.1103/PhysRevLett.104.207401.
[61] M.J. Biercuk, M.C. Llaguno, M. Radosavljevic, J.K. Hyun, A.T. Johnson, J.E. Fischer, Carbon nanotube composites for thermal management, Appl. Phys. Lett. 80 (2002) 2767–2769, https://doi.org/10.1063/1.1469696.
[62] B.S. Flavel, M.M. Kappes, R. Krupke, F. Hennrich, Separation of single-walled carbon nanotubes by 1-dodecanol-mediated size-exclusion chromatography, ACS Nano 7 (2013) 3557–3564, https://doi.org/10.1021/nn4004956.
[63] H. Li, G. Gordeev, O. Garrity, S. Reich, B.S. Flavel, Separation of small-diameter single-walled carbon nanotubes in one to three steps with aqueous two-phase extraction, ACS Nano 13 (2019) 2567–2578, https://doi.org/10.1021/acsnano.8b09579.